Physics – Uspekhi **60** (9) 886 – 901 (2017)

REVIEWS OF TOPICAL PROBLEMS

PACS numbers: **07.35.+k**, 61.50.Ks, **62.50.–p**, 64.70.K–, **67.63.–r**, 67.80.F–, 67.80.ff, 74.62.Fj, 81.40.Vw

Hydrogen and its compounds under extreme pressure*

A N Utyuzh, A V Mikheyenkov

DOI: https://doi.org/10.3367/UFNe.2017.02.038077

Contents

Abstract. In the last two or three years, significant advances in the study of hydrogen and its compounds under extreme conditions (ultrahigh pressures over a wide temperature range) have notably changed the hydrogen phase diagram, provided a breakthrough in understanding hydrides' behavior under pressure (as exemplified by the discovery of high-temperature superconductivity in hydrogen sulfide), and, finally, enabled achieving cold metallization of hydrogen. The situation prior to the 2010s is reviewed in brief and more recent work is examined in detail. While the primary focus is on experimental research, mention is also made of the theoretical and numerical work it stimulates.

Keywords: hydrogen, deuterium, high pressures, phase diagram, superconductivity

1. Introduction

In 1935, Wigner and Huntington [1] predicted that solid molecular hydrogen should become atomic and metallic if compressed under the pressure of 25 GPa (let us recall that 1 GPa = 10 kbar) at low temperatures. During the following several decades, a number of publications were issued considering the calculations of thermodynamic potentials for molecular and metallic hydrogen phases in order to define the pressure at which the transition to the metal phase occurs. In a series of articles by Abrikosov on the theory of highly compressed materials [2–5], the properties of the hydrogen metallic phase under pressure were analyzed as well. The equation of state for the molecular phase was calculated by Trubitsyn [6, 7] employing a simple analytical expression for the intermolecular interaction potential, which included van der Waals attraction and short-range repulsion.

Investigations of hydrogen under pressure were stimulated by the predictions of the peculiar properties of its metallic phase [8–11]. Of specific interest was the possibility of high-temperature superconductivity, which can be seen already from the simplest estimate: the Debye temperature in the pre-exponential factor of the Bardeen–Cooper–Schrieffer (BCS) expression for the superconducting transition temperature T_c is inversely proportional to the square root of the atomic mass and reaches a record-high value for hydrogen: $\Theta_D = 3.5 \times 10^3$ K. In 1968, Ashcroft [8] considered the expression for the exponential argument and predicted that the superconducting transition temperature in metallic hydrogen under the hardest upper estimation should be at least several dozen kelvins. A more detailed estimate appeared a year later [12], but it led to a broad range of possible temperatures T_c from 100 to 200 K. A survey of the latest estimates resulting in even higher values of T_c can be found in review [13].

The broad range of predicted values for T_c as well as for other characteristics can be explained, in particular, by the low applicability of standard solid-state calculation methods due to the absence of nucleus screening by inner electrons. Moreover, there is competition among several structures with close energies, which leads to many different scenarios for hydrogen's behavior under pressure [10]. These circumstances

A N Utyuzh Vereshchagin Institute of High Pressure Physics, Russian Academy of Sciences, Kaluzhskoe shosse 14, 108840 Troitsk, Moscow, Russian Federation
A V Mikheyenkov Vereshchagin Institute of High Pressure Physics, Russian Academy of Sciences, Kaluzhskoe shosse 14, 108840 Troitsk, Moscow, Russian Federation; Moscow Institute of Physics and Technology (State University), Institutskii per. 9, 141700 Dolgoprudnyi, Moscow region, Russian Federation; National Research Center 'Kurchatov Institute', pl. Akademika Kurchatova 1, 123182 Moscow, Russian Federation
E-mail: mikheen@bk.ru

Received 12 August 2016, revised 19 February 2017
Uspekhi Fizicheskikh Nauk **187** (9) 953 – 970 (2017)
DOI: https://doi.org/10.3367/UFNr.2017.02.038077
Translated by A L Chekhov; edited by A Radzig

* This review presents an extension of the talk by the authors for the scientific session of the Physical Sciences Division of the Russian Academy of Sciences, "Old and new ideas in phase transition physics," which was held on December 21, 2016 (see *Phys. Usp.* **60** 948–957 (2017); *Usp. Fiz. Nauk* **187** 1021 (2017)). (*Editor's note.*)

somewhat limit the predictive capacity of theory and make the experimental approach of main importance.

The current state of experimental and theoretical research on hydrogen is presented in reviews [13–15]. Reviews [16–18] are devoted to hydrogen investigations by the means of dynamic compression methods. Papers [19, 20] describe the method of laser compression of the samples, which were preliminarily compressed statically. And, finally, review [21] provides information on investigations of hydrogen's solid phases and melting curves, which were performed throughout recent decades in diamond anvil cells.

Due to the appearance of many unusual properties in hydrogen, its investigation under extremely high pressures is one of the most important lines of inquiry in solid state physics. Moreover, reaching the hydrogen metallic state is one of the main concerns of physics in general [22, 23].

Besides hydrogen, a great deal of attention was paid to hydrides. In 2004, Ashcroft [24] assumed that dense hydrides of group-IV elements are prospective candidates for hydrogen metallization under pressures that would be much lower than in the case of pure hydrogen, because hydrogen in hydrides is already subjected to 'chemical pressure'. The modern state of research on superconductivity in hydrogen-rich materials under extreme pressure is presented in review [25].

Investigations of hydrogen and hydrides under extreme conditions had been intensively performed before, but in 2014–2016 this field of research turned out to be exceptionally fruitful. A number of experimental papers quickly led to significant changes regarding the positions of melting curves and plasma phase transition lines in the hydrogen phase diagram. Experimental investigations of superconductivity in hydrogen sulfide stimulated the publication of a large number of theoretical papers. The possibilities of the experiment were significantly improved both in the investigations with a diamond anvil and in those using dynamic compression.

The goal of this review is a short discussion of the most recent results which have led to significant changes in the hydrogen phase diagram and to breakthroughs in research on superconductivity in hydrides. In Section 2, we describe the hydrogen phase diagram proper; in Section 3, we review monosilane, and in Section 4 we address the issue of the very recently discovered high-temperature superconductivity in hydrogen sulfide under pressure. In the Conclusions (Section 5), we briefly summarize the results obtained over recent years.

2. Hydrogen phase diagram

As mentioned in the Introduction, more than 80 years ago E Wigner and H B Huntington theoretically predicted that solid molecular hydrogen should become atomic and metallic when compressed to the pressure of 25 GPa at a low temperature. Later on, due to the study of Jupiter and other giant planets, a similar transition became of interest in liquids at low temperatures in the region, which is directly above the melting curve. This interest was also caused by the possibility of achieving very high pressures using dynamic compression methods. Consequent theoretical papers investigated these two transition paths to the metallic state: isothermal compression up to the formation of the solid atomic metallic phase, and liquid hydrogen metallization under compression — the liquid–liquid insulator-to-metal transition (LLIMT).

The hydrogen phase diagram significantly evolves as new experimental and theoretical data are obtained [13, 21, 23]. As a starting point, we will further explore the hydrogen phase diagram based on experimental and theoretical work, plotted in Fig. 1. Theoretical investigations of the hydrogen melting curve depending on the pressure have predicted the existence of a maximum in this line [26]. Extrapolation of the obtained melting curve (calculations [26] are valid only for high temperatures) assumes that hydrogen in the ground state can be liquid (atomic and metallic) under multimegabar pressures (see the dashed line in Fig. 1). Simulations [27] support this extrapolation. At even higher pressures, atomic hydrogen should solidify again.

Progress in experimental methods, especially of the ones with a diamond anvil, allowed performing hydrogen investigations under pressures of up to 400 GPa. At the same time, progress in dynamic compression methods allowed the observation of liquid hydrogen metallization in the previously inaccessible temperature range $T = 1100$–1600 K, which is located below the assumed position of the critical point (see Fig. 1, and also Fig. 10 in Section 2.3). Experimental and theoretical investigations led to an extended, rich, and interesting hydrogen phase diagram, which includes stability regions for liquid molecular hydrogen and six

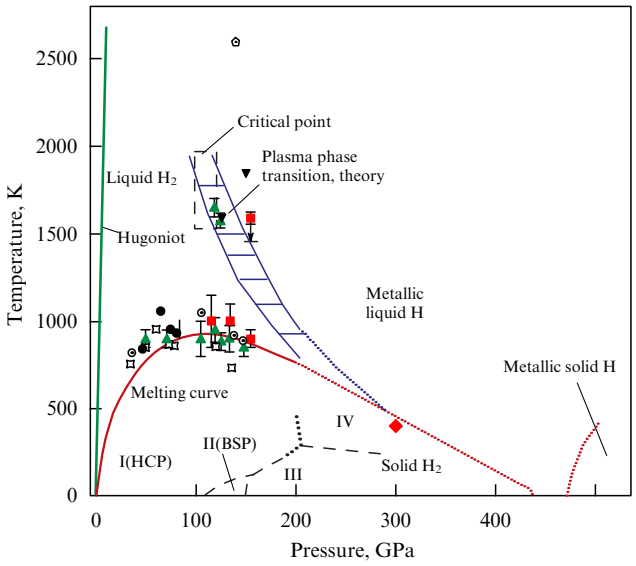

Figure 1. (Color online.) Hydrogen phase diagram presenting data for the melting and LLIMT curves. The LLIMT is represented by two curves obtained in recent calculations [26, 28–31] that are connected with horizontal segments. Predicted position of the LLIMT critical point, which is different in these papers, is indicated by a dashed rectangle. The diagram also shows experimental data in the LLIMT region. Green triangles and red squares are the results of paper [32], and two black triangles from paper [33] (for deuterium) correspond to molecular and liquid atomic phases. Unfilled circles show the results of paper [34], black circles — [35], unfilled squares — [36], and pentagon — [37]. Diamond symbol is the result of calculations using quantum Monte Carlo method [27]. (See also Figs 4, 5, and 7 below.) Low-temperature phase I has a hexagonal close-packed (HCP) structure formed by freely rotating molecules. It is adjacent to phase II — the broken symmetry phase (BSP), where the rotation of molecules is restricted. At low temperature and pressure of about 160 GPa, the transition from phase II to phase III occurs. The experiment also indicates the existence of the phase IV for temperatures above several hundred degrees and pressures above 220 GPa. The structures of phase III and IV are not yet defined, and they are distinguished only by Raman spectra. (Taken from paper [32].)

different phases of solid molecular hydrogen, as well as regions where solid and liquid atomic states can exist.

Sections 2.1–2.3 analyze the hydrogen phase diagram and new experimental and theoretical results, which were obtained using two paths to the metallic state. We discuss the papers published over the last few years regarding studies of hydrogen under static and dynamic compression. The results of these investigations have led to a significant modification of the phase diagram: changes in the positions of the melting curve, the LLIMT line, and the regions of different solid hydrogen states under maximal static pressures.

2.1 Melting curve of hydrogen

At normal pressure, hydrogen crystallizes in a hexagonal close-packed (hcp) lattice at a temperature of 14 K. First investigations of the melting curve were performed in piston–cylinder cells. The capabilities of such cells are limited by the pressure $P = 2$ GPa [39, 40]. In order to achieve higher pressure, diamond anvil cells (DACs) and resistance heating were exploited, while the following methods were applied to register melting: visual observation (for P below 7.7 GPa) [41, 42], $P-T$ scanning (for P below 15 GPa) [43], and Raman spectroscopy measurements (for P below 44 GPa) [43, 44]. In paper [44], the melting was registered by the jumps in the temperature dependence of the vibron Raman frequency.

This was the state-of-the-art by the early 2000s. Later experiments, which took advantage of laser heating and Raman spectroscopy, have pushed the pressure limit up to 150 GPa [34, 36]. However, laser heating has inevitable deficiencies (large temperature gradients and presence of chemical reactions), which lead to uncertainty in melting registration and large temperature errors of experimental points, so this does not prove the decrease in melting temperature with increasing pressure. Figure 2 demonstrates that the dashed line (decreasing melting temperature with the pressure increasing) and the solid line (saturating dependence) approximate the experimental data with similar errors.

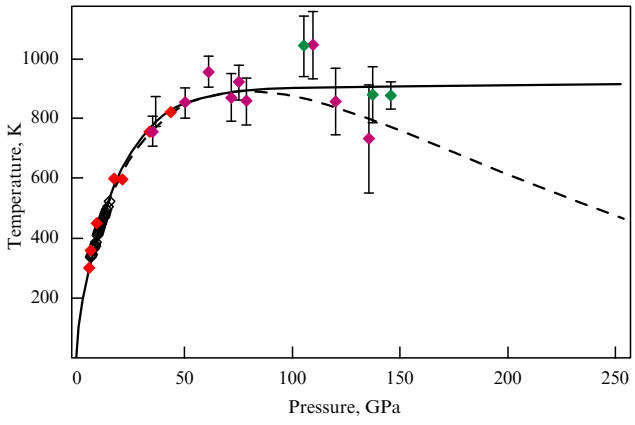

Figure 2. (Color online.) Data from previous years regarding the hydrogen melting curve from papers with resistance [43, 44] and laser [34, 36] heatings. Black diamonds show results from Ref. [43], red — [44], green — [34], and magenta — [36]. Data for melting during the laser heating were obtained under pressures below 146 GPa, but the experimental points are greatly scattered and the measurement errors are large. All data can be adequately fitted both with the Kechin expression (dashed line), demonstrating the melting temperature decrease with increasing the pressure, and with another melting dependence (solid line) with a very weak temperature increase at high pressures. (Taken from paper [38].)

The measurement method was improved in paper [38] published in 2015. The authors of this work made their own design of the diamond anvil cell. After sealing gaseous hydrogen at $P = 0.2$ GPa, the pressure was heightened to the desired level at a temperature of 300 K. Fifty experiments were performed in the pressure range from 3 to 360 GPa. The pressure was defined using both the diamond edge Raman frequency with calibration [45] and the hydrogen vibrational mode frequency from measurements [46]. The experiments were carried out for $T < 900$ K with resistance heating, because in this case the temperature can be measured with a high accuracy, unlike laser heating, and the signal-to-noise ratio of Raman measurements is high, too. Raman spectroscopy studies were performed using excitations at the wavelengths of 514.14 and 647.1 nm. The CCD (charge-coupled device) matrix used in the experiments was designed for operating in the visible range; therefore, for excitations at $\lambda = 647.1$ nm, the hydrogen vibrational mode with a frequency of about 3500 cm^{-1} was significantly weaker than the low-energy lattice modes. However, exactly this wavelength was adopted in most of the experiments, because the excitation at $\lambda = 514.15$ nm gives rise to fluorescence of strained diamond anvils, which masks the Raman signal.

In paper [38], the experimental results were approximated using the Kechin empirical equation [47] (Fig. 3). The figure shows results for pressures below 200 GPa and temperatures up to 800 K, for pressures between 200 and 275 GPa and temperatures up to 500 K, and for pressures up to 325 GPa and the temperature $T = 300$ K. Theoretical calculations of the melting curve [26, 30, 31, 48, 49] qualitatively agree with the experimental results [38].

Measurements [38] restrict the possible positions of the melting curve in the hydrogen phase diagram and allow discussing the existence of the minimum in the melting curve

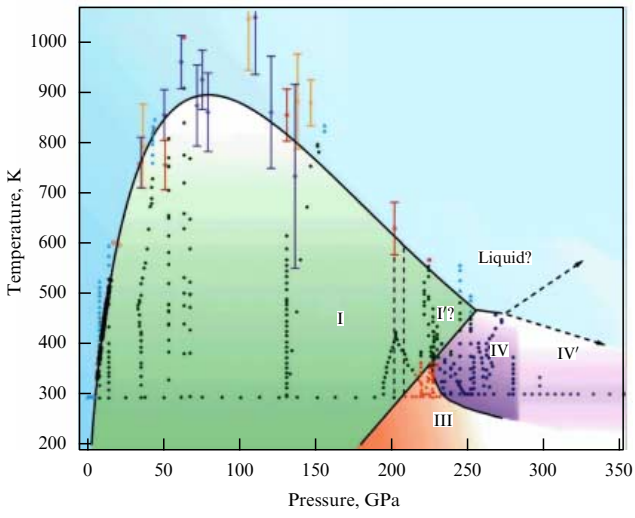

Figure 3. (Color online.) Hydrogen melting curve for pressures up to 325 GPa. The curve was obtained by fitting the experimental data from paper [38] and previous work with a Kechin dependence. Green circles — solid state, and blue triangles — liquid phase. Previous data are presented with diamonds of different colors: light-brown — Ref. [44], magenta — [36], yellow — [34], red — calculations [26], and black at low pressures — [43]. The boundary between phases I–III is taken from papers [38, 46]. Dashed lines are possible continuances of the transition curve (or the melting curve). Curves between phase regions have an uncertainty of ±10 GPa. (Taken from paper [38].)

and the existence of the liquid ground state [10, 50] possessing extraordinary properties [50].

Possible continuations of the melting curve plotted in Fig. 3 forbid the liquid state with $T < 300$ K at pressures less than 400 GPa. Recent theoretical investigations [48] predict an almost horizontal melting curve in the pressure range from 300 to 500 GPa. In principle, the liquid phase can be realized in the pressure region above 500 GPa under the dissociation of hydrogen molecules (due to zero-point vibrations).

In the latest theoretical work, where such effects were taken into account, the liquid ground state is either not found for P below 600 GPa [48] or is placed in the pressure region above 900 GPa in the wake of the predicted solid atomic phase [49]. In order to solve these problems, a significant improvement is needed in the methods, which allow for direct registration of hydrogen melting, such as X-ray diffraction or Brillouin spectroscopy.

2.2 Crystalline structures of H_2

Defining the hydrogen phase diagram is one of the main issues for both theory and experiment. Several crystalline phases of molecular hydrogen have been observed in diamond anvil cells at pressures below 300 GPa [21] (Fig. 4).

Low-temperature phase I has an hcp structure, which is formed by freely rotating molecules. Phase I is adjacent to phase II with broken symmetry, and the rotation of molecules in it is restricted. The transition pressure significantly decreases as the isotope's mass is increased, being also dependent on the total spin of the molecules. At a low temperature and for a pressure of about 160 GPa, a phase II to phase III transition takes place. Experiment also evidences the existence of phase IV at temperatures above several hundred degrees and pressures above 220 GPa [46]. A density functional theory was applied to study phase IV in paper [52].

Experiments do not allow defining the atomic structure of solid hydrogen at high pressures, because hydrogen weakly scatters X-ray radiation, but they can result in establishing some limitations on possible structures — infrared and especially Raman spectroscopy provide valuable information on the vibrational modes. Since the experimental results are not enough in order to define phase II, III, and IV structures, their properties are mostly determined from the calculations.

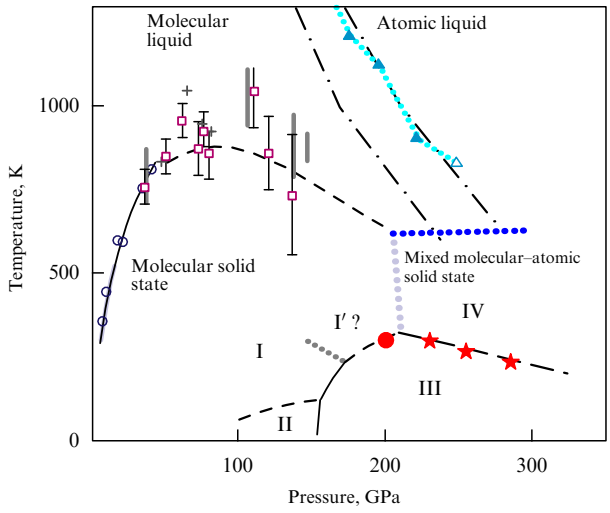

Figure 4. (Color online.) Hydrogen phase diagram. I–II and I–III phase transition curves for normal hydrogen are taken from paper [21]. Different symbols correspond to data from different experimental investigations, reviewed in Ref. [21]. (Taken from paper [21].)

Reference [13] gives a review of calculation methods applied for the description of hydrogen properties under extremely high pressures and temperatures. Over recent years it is common to use *ab initio* modeling methods, among which the most popular are the density functional theory (DFT) and quantum Monte Carlo (QMC) method.

Our knowledge about the atomic structure is mostly based on DFT calculations. Structure candidates for every experimentally examined phase are chosen by comparing the Raman spectra obtained for low-energy structures using the DFT method with the experimental spectra. Several structure candidates were proposed based on the DFT analysis, but it should be emphasized that none of these structures can be considered the uniquely correct one. The DFT predicts that the metallic structures are energetically most favorable in a wide pressure range up to 400 GPa. However, as is known from experiments, hydrogen behaves in this region as nonmetal.

In a numerical investigation [53] performed in 2015 using the diffusive quantum Monte Carlo method, it was found that metallic structures are energetically unfavorable, and the H_2 phase diagram was predicted. The theoretical phase diagram obtained in Ref. [53] qualitatively agrees with experimental results, thus pointing to the fact that $P2_1/c$-24, C2/c-24, and Pc-48 structures take the part of satisfactory models for phases II, III, and IV. These model structures well describe experimental spectra of infrared absorption and Raman scattering. However, there is a discrepancy with experimental data regarding the position of the boundary between phase II and phase III at low temperatures.

The hydrogen phase diagram at pressures above 200 GPa will undergo significant modification when accounting for the results of the recent experimental work [38] described above (see Fig. 3). Using diamond anvil cells with resistance heating and Raman spectroscopy studies, the authors discovered a new phase IV′ and a new triple point between phases I′, IV and liquid [38]. It was reported that hydrogen remains molecular in the vicinity of this point.

Based on Raman scattering measurements performed in 2016, the authors of paper [54] provided evidences of the possible existence of a new hydrogen phase (dubbed phase V in Ref. [54]) in the pressure region 325–388 GPa and temperature region 300–465 K (Fig. 5). These evidences were observed in H_2 and HD, but not in D_2, and include significant weakening of Raman vibron activity, changes in pressure dependence of this vibron, and the disappearance of several low-frequency Raman modes.

Yet another paper published in 2016 [56] led to a further modification of the hydrogen phase diagram. Phase transitions were defined based on measuring the Raman spectra of the vibron (Fig. 6). The boundary between phases I and III was reconsidered and continued up to temperatures above room temperature, regions of phases IV and V existence were established, and the low-temperature phase diagram of hydrogen for $P < 380$ GPa was significantly clarified (Fig. 7).

Evidences of the existence of a new phase (phase VI) were observed for the highest-achieved pressures of 360–370 GPA at temperatures below 204 K [56]. This phase was discovered in work [56] by the disappearance of phase-V Raman modes at pressures of 360–370 GPa and temperatures below 204 K. The narrow Raman line of 300 cm^{-1} characteristic for phase V is observed during cooling from 282 to 204 K and vanishes at

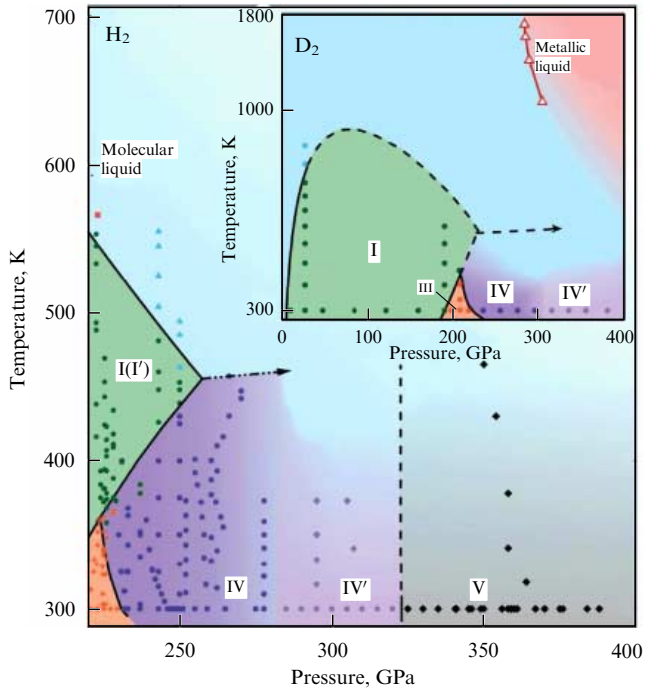

Figure 5. (Color online.) Suggested hydrogen phase diagram for pressures up to 400 GPa. Colored symbols in the pressure region below 300 GPa for I–IV phases correspond to paper [38]. The results obtained in paper [54] are indicated by black diamonds (phase V). The deuterium phase diagram is plotted in the inset. Red triangles (data from paper [55]) separate regions of metallic and semiconducting liquids. (Taken from paper [54].)

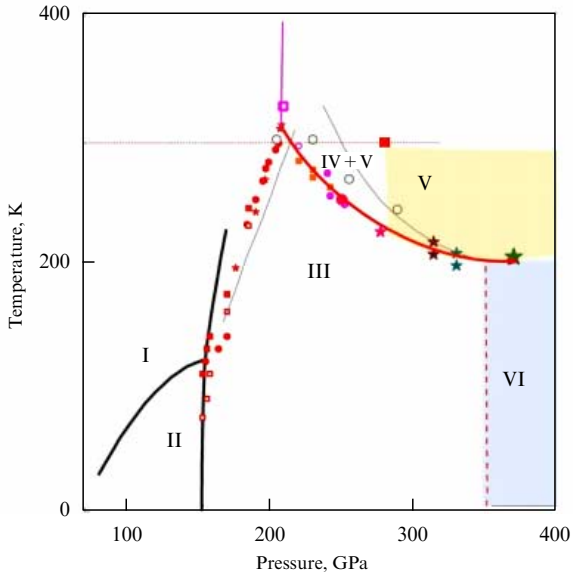

Figure 7. (Color online.) Hydrogen phase diagram. Phases I–VI are indicated. Horizontal line and large red square designate the pressure increase at room temperature and the phase transition [57]. Colored symbols (red, orange, and bright pink) label phase transitions disclosed by the changes in Raman and infrared spectra according to data from paper [56]. The position of the triple point defined from these data is $P = 208$ GPa and $T = 305$ K. It seems that in the pressure region of 220–270 GPa there is a mixture of phases IV and V. (Taken from paper [56].)

203 K and for lower temperatures. A significant decrease in resistance and the disappearance of the photoconductivity response were simultaneously detected.

In both papers [54, 56], the authors made assumptions that the metallic state can be reached at pressures around 400 GPa. These assumptions, however, have not been confirmed yet in independent studies.

Let us mention also a theoretical prediction about the transfer of phase IV to the molecular metallic phase with the Cmca-4 structure at pressures above 360 GPa [58]. However, at such pressures monatomic metallic phases become competitive and, moreover, for such parameters, it is important to take into account quantum effects [59]. Approaches to higher pressures, $P \lesssim 400$ GPa, are described in preprints [60, 61] (Fig. 8).

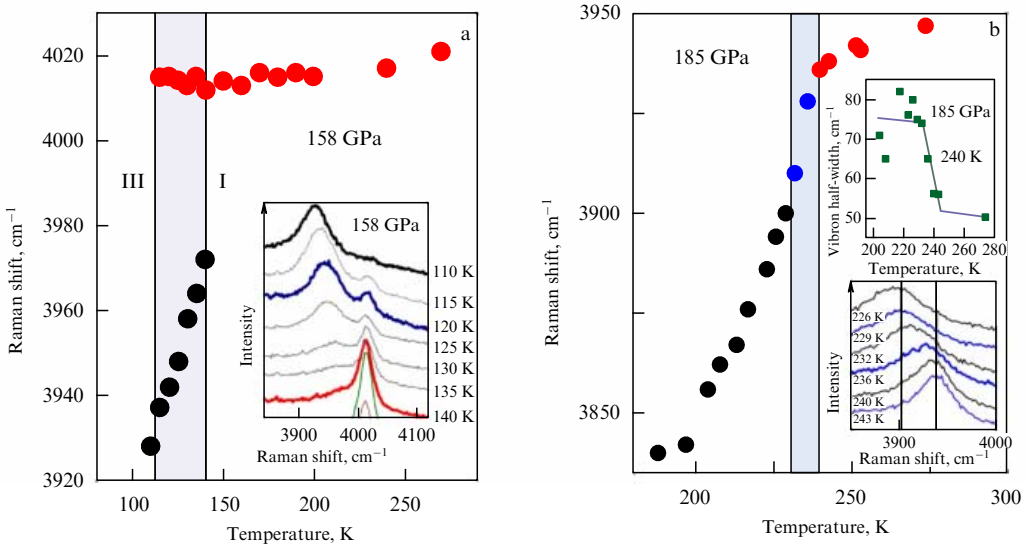

Figure 6. (Color online.) Transitions from phase I to phase III at different pressures defined from Raman spectrum measurements of the molecular hydrogen vibron. (a) During cooling from room temperature (under 158 GPa pressure), the vibron frequency remains almost constant for $T < 110$ K. Phase II vibron at lower frequency appears at a temperature of 140 K. In the temperature region of 110–140 K, phases I and III coexist. The phase III vibron frequency rapidly increases with temperature, and its half-width decreases, which can be seen in the inset. (b) For a pressure of 185 GPa, the I–III phase transition is defined by the change in the slope of the curve at 240 K and by a substantial change in the temperature dependence of the vibron frequency. The frequency jump and the increase in the vibron half-width (see inset) during this transition are significantly smaller than for 158 GPa. Red dots correspond to phase I, black ones to phase III, and blue ones to the region of phases I and III coexistence. (Taken from paper [56].)

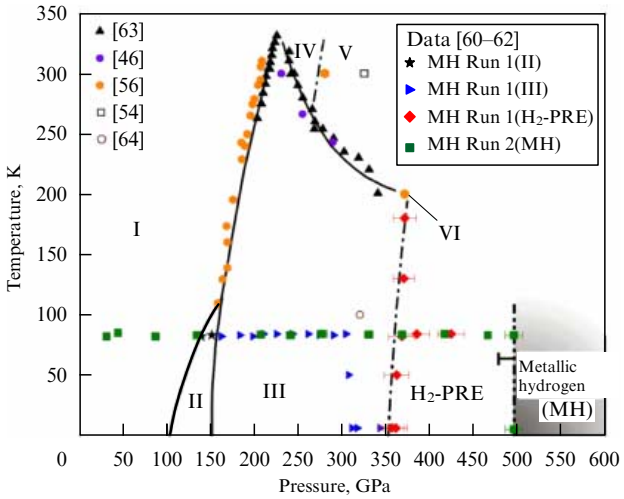

Figure 8. (Color online.) Portion of hydrogen $P-T$ phase diagram for low-temperature path towards solid metallic hydrogen (MH) based on all experimental results up to the beginning of 2017. Several experimental runs from Refs [61, 62] are presented, as is the data obtained in the same group [60] for the H_2-PRE phase (designations are shown in the upper right-hand part of the figure). The diagram also depicts the results from the following papers (designations are shown in the upper left-hand part of the figure): [63, 46, 56], [54] (unconfirmed report on the phase transition), and [64] (early report on the observation of darkened hydrogen). (Taken from papers [61, 62].)

In Ref. [60], a new phase was discovered at $P \approx 350$ GPa and $T = 5$ K and named by the authors H_2-PRE, assuming that it precedes the transition to metallic state (at higher temperatures, this phase was called phase VI in work [56]). At maximum experimental pressure $P \approx 420$ GPa [60], the sample darkened in the visible region, but there was no evidence of it being metallic.

And, finally, the most important recent achievement was claimed in the report on the creation of crystalline metallic hydrogen (see preprint [61] and its journal edition [62]). The authors of Refs [61, 62] have improved the methodology for working with diamond anvils in order to achieve significantly higher pressures. As the pressure was increased, the sample first transformed from transparent to opaque and then made transition to the state with metallic luster. The transition pressure was defined from the diamond phonon Raman shift using a low-power laser, which resulted in the pressure $P = 495 \pm 13$ GPa (the pressure was measured at $T = 83$ and 5.5 K, and appeared to be almost independent of the temperature).

Analysis of the reflection coefficient measurements using the Drude model allowed an estimation of the plasma frequency and electron density. The latter at the transition pressure corresponds to one electron per atom.

Summing up, the authors of Refs [61, 62] believe that their experiment resulted in the formation of atomic metallic hydrogen, so the Wigner and Huntington prediction made in 1935 is confirmed.

2.3 Liquid–liquid phase transition in dense hydrogen

The second possible path to hydrogen metallization can be realized at high values of temperature and pressure. This is related to the well-known problem of nonmetal-to-metal transition in liquid or — for higher temperatures — in plasma. Landau and Zeldovich [65] more than 70 years ago suggested the possibility of nonmetal-to-metal transition in liquid mercury and showed from the most general considerations that this should be a first-order transition. A metal-to-insulator transition 'not in a crystal', later dubbed the plasma phase transition (PPT), in dense plasma was first considered by Norman and Starostin [66].

At the end of the 20th century, liquid metallic hydrogen was observed at a temperature of about 2500 K and a pressure of 140 GPa [37] which is much lower than the transition pressure theoretically predicted for solid hydrogen. This discovery initiated intensive experimental and theoretical investigations.

The authors of papers [28, 31] predicted in liquid molecular hydrogen at high pressures the curve of first-order liquid–liquid transition to atomic metallic hydrogen. LLIMT is accompanied by hydrogen molecule dissociation and heat absorption. It is assumed that Saturn's and Jupiter's magnetic fields are generated by the convective motion of dense conducting hydrogen, which can be monatomic fluid hydrogen dissociated from diatomic dense fluid.

The nature of plasma transition in hydrogen and deuterium was investigated both experimentally and theoretically. In Ref. [30], the calculations were performed using quantum modeling by means of both the density functional theory and quantum Monte Carlo method. The results indicated a first-order transition in liquid hydrogen between the molecular state with low conductivity and the atomic state with high conductivity. As estimated [30], the critical point in the transition curve is located at a temperature of about 2000 K and pressure of 120 GPa.

LLIMT has been experimentally investigated applying various methods. There are reports [37, 67] of the observation of electric conductivity in hydrogen and deuterium at high pressures and temperatures using reverberating shock waves, when the conditions for P and T are simultaneously fulfilled over a time of 100 ns. In the papers mentioned, the electric conductivity was demonstrated to increase up to four orders of magnitude in the pressure range of 93–140 GPa and to have an almost constant value, corresponding to metallic liquid, at pressures from 140 to 180 GPa. The calculated temperature ranged from 2500 to 3500 K. These data are explained as a continuous transition from a semiconducting liquid to a diatomic metallic liquid at $P = 140$ GPa and $T = 3000$ K.

The authors of Ref. [33] investigated quasi-isentropic explosive compression of deuterium and registered a jump in the density at high P and T, which was interpreted as a PPT observation. The hydrogen density was defined by the sample radius value, which was obtained using high-speed X-ray shooting, and the temperature was calculated applying plasma models. It was noted that the observed jump in the density was in the parameter region, for which other authors have registered a conductivity increase by five orders of magnitude. Data from paper [33] are shown in Fig. 1.

In papers [19, 20], shock waves were generated by laser pulses in hydrogen and deuterium samples, preliminarily compressed in a diamond anvil cell to pressures of 0.7 and 1.2 GPa. The measurements were performed in the final pressure range of 40–175 GPa and for temperatures of 5000–20,000 K. By measuring the shock wave speed and thermal radiation, the authors obtained data related to the equation of state (pressure, density, temperature) in the region of dense fluid at pressures up to 175 GPa. The measurements of the optical reflection indicate the onset of the temperature transition to a conducting fluid state. The main result of these papers is that the transition to the

conducting state starts at temperatures which are twice as high as the LLIMT temperatures predicted in *ab initio* calculations using quantum molecular dynamics methods [68, 69]. It should be noted that the experimental data in Refs [19, 20] are related to the temperature range where the main factor for conductivity is temperature. Such temperatures are significantly larger than that of the LLIMT critical point obtained in *ab initio* calculations (see Fig. 1).

In order to study the LLIMT (transition to liquid atomic metallic hydrogen), the authors of Ref. [32] heated hydrogen using a pulsed laser in the megabar pressure range in a diamond anvil cell. The pressure was measured at room temperature by a ruby fluorescence and the position of the Raman phonon edge in diamond. The peak temperature was defined from the time-averaged radiation spectrum by fitting it with the black-body radiation curve. The samples were heated to temperatures significantly exceeding the melting curve temperature. The experiment showed a plateau in the temperature dependence on the laser power in the region where, under normal conditions, one would observe a monotonic increase. This anomaly in the heating curve agrees with the theoretical predictions of LLIMT and appears as an experimental evidence (though an indirect one) of such a transition.

In a later (2015) analogous experiment in a diamond anvil cell with laser heating [70], the temperature dependence on the laser power showed a plateau once again. Observed anomalies in the heating efficiency were related to a phase transition from diatomic liquid hydrogen to monatomic liquid hydrogen (LLIMT) in the pressure range from 82 to 106 GPa. In check experiments without hydrogen loading, anomalies in the heating efficiency were not observed. Analysis of X-ray data and Raman scattering measurements before and after the experiments did not reveal any signs of a chemical reaction of hydrogen with surrounding materials.

In paper [71] published in 2016, the observation of similar plateaus was complemented with measurements of the optical properties of hot dense hydrogen in the pressure range of 110–170 GPa. The results indicated a first-order transition to a metallic phase. The hydrogen was heated by pulses from a neodymium laser with 280 ns duration, which is sufficient to reach local thermal equilibrium, but not enough for hydrogen diffusion into anvils. The hydrogen sample surface was heated by the pulse up to the temperature of 2200 K. However, the pulse energy was so small that the diamond anvils and the larger part of the sample had a temperature on the order of room temperature. The temperature was defined by thermal radiation, similarly to the method applied in paper [32] and described above. The measurements were performed using laser lines with wavelengths of 514, 633, 808, and 980 nm. The curve of the transition to the metallic state was defined by an abrupt decrease in the transmission coefficient and an increase in the reflection coefficient (estimates were made using the Drude model). Observed heating efficiency plateaus, which can be explained by the existence of latent heat, also point in favor of a first-order phase transition. The phase transition curve separating insulating and high-temperature conducting metallic phases has a negative slope, which agrees with theoretical PPT model predictions.

Plasma phase transition temperatures found in papers [70, 71] are presented in Fig. 9. The results are in good agreement with previously assumed LLIMT boundaries [32]. However, they set up a more narrow range for the boundaries of this phase transition and result in a higher temperature of the critical point than the value predicted by theoretical calculations [30].

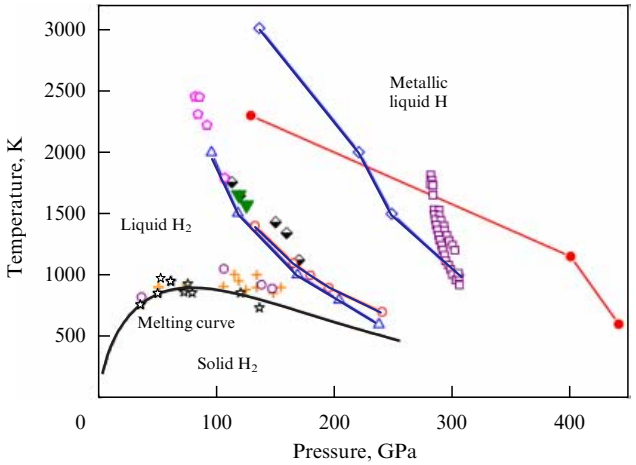

Figure 9. (Color online.) Hydrogen $P-T$ diagram. Experimental data for the melting curve are as follows: black line — [38], circles — [34], stars — [36], and crosses — [32]. Experimental data for LLIMT: lilac squares — [55], black and white diamonds — [72], green triangles — [32], and pink pentagons — [70]. Results of theoretical calculations for LLIMT: blue triangles — [30], blue diamonds — [73], open circles with pink contour — [29], and red (filled) dots — [74].

All the experimental evidence of the existence of LLIMT in hydrogen and deuterium — changes in conductivity [37, 67] and density [33], a plateau in the temperature dependence on the heating power [32, 70], the results of the analysis of the optical properties [71] — is indirect. The definitive signs of a phase transition in molecular hydrogen and deuterium are the significant changes in the Raman spectrum and in electric and heat conductions [36, 37]. Therefore, the location of a plasma phase transition in hydrogen is still under discussion.

The results for the LLIMT curve location obtained in paper [55] in 2015 (Fig. 10) highly deviate from the results described above. In a series of experiments [55], liquid deuterium was dynamically compressed in a Z-machine at Sandia National Laboratories [75]. In this setup, using a strong magnetic field, a flat metallic plate is accelerated up to speeds which result in providing megabar pressure. The setup allows strong pulsed currents (around 20 MA) and magnetic fields up to 500 T to be generated. Electric current and a magnetic field create, in turn, a pressure of a few hundreds of GPa in time periods on the order of 1 μs. If the experimental configuration is correctly designed and the current pulse is properly shaped, the deuterium sample compresses to the pressure of 300 GPa, while the temperature stays below 1800 K. These experiments have shown an abrupt increase in the reflection coefficient, which corresponds to a jump-like conduction increase in the pressure range of 280–305 GPa. This increase was explained in paper [55] as evidence of jump-like LLIMT governed by the density.

Since experiment [55] is critically important, we will describe it in more detail. The sample of liquid deuterium was condensed from gas into a cryogenic cell at $P = 124$ kPa and $T = (22 \pm 0.1)$ K. A schematic of the cryogenic cell is shown in Fig. 11. The cell is located at a small distance from an aluminum electrode. The initial current pulse accelerates the aluminum plate. After colliding with the front plate of the cryogenic cell, a shock wave is produced, and it causes a series of reflections-reverberations, which result in a stepwise loading of the deuterium sample.

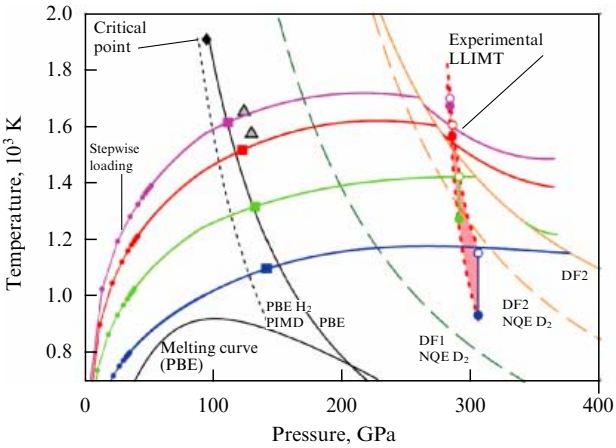

Figure 10. (Color online.) Deuterium $P-T$ diagram. Melting curve indicated in diagram is calculated in Ref. [30] using the Perdew–Burke–Ernzerhof (PBE) semilocal density functional. Theoretical LLIMT curves are as follows: black — PBE [30], black dashed — PBE + PIMD, green dashed — DF1 + NQE [55], orange — DF2 [55], and orange dashed — DF2 + NQE [55]. Designations: PIMD — path integral molecular dynamics; DF1(+NQE), DF2(+NQE) — different types of nonlocal density functionals, and NQE — nuclear quantum effects. Experimental data: grey triangles label the results from Ref. [32]; experimental $P-T$ trajectories from paper [55] are shown to saturate by colored solid curves, and colored squares for pressures from 120 to 150 GPa show where deuterium becomes opaque, when the bandgap energy decreases to a 2.1 eV. Region indicated with red color marks the experimentally defined position of LLIMT. (Taken from paper [55].)

The consequent current increase results in the origin of a ramp compression wave in the cryogenic cell and the deuterium sample is further compressed along the isentrope to peak pressure (300 GPa) and density (2 g cm^{-3}) values. By changing the impact plate collision velocity, one can find itself in isentropes corresponding to different temperatures, which allows studying a broad $P-T$ range (almost horizontal color lines in Fig. 10). The state of the liquid deuterium sample was diagnosed by two fiber sensors (see Fig. 11). Velocity interferometer systems for any reflector (VISAR) measured the velocity of aluminum/deuterium and deuterium/LiF (under the reflection from an aluminum coating on an LiF window) interfaces (Fig. 12). The wavelength of the laser radiation was 532 nm. Another sensor measured the spectral- and time-resolved reflections using a spectrometer with a wavelength range of 450–650 nm connected to a camera.

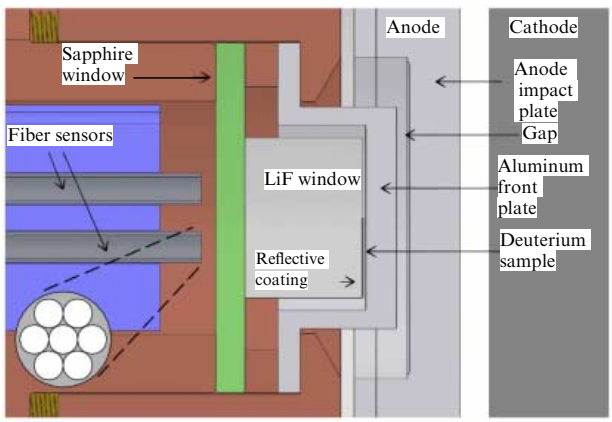

Figure 11. (Color online.) Schematic of a cryogenic cell. (Taken from Ref. [55].)

It is interesting to compare paper [55] with [37, 67]. Both groups used dynamic compression in order to reach the region of the hydrogen phase diagram, which corresponds to high densities and low temperatures. However, the authors of Ref. [37] were limited in the final states by the possibilities of shock-wave experiments with reverberation. In paper [55], lower initial compression was combined with subsequent linear compression, so higher densities were obtained at lower temperatures. Both groups measured P, while the density and temperature were defined using the deuterium equation of state and numerical modeling.

The authors of Ref. [67] measured DC conductivity in the final state of a shock-wave reverberation and they were forced to perform many experiments at successively higher densities and temperatures, which complicated the separation of density and temperature contributions to the conductivity increase.

The authors of Ref. [55], on the contrary, directly observed a deuterium sample during the whole compression process and could measure the optical properties as a function of density at a relatively constant temperature (Fig. 13) (see also Fig. 10). These measurements revealed a sharp increase in the optical reflectance, which agrees with the conductivity increase obtained from DFT calculations and in the maximum corresponds to the conductivity values given in Ref. [37]. The pressure at which this sharp increase originates is almost independent of the temperature, which supports the final conclusion of paper [55] that deuterium indeed experiences a transition to a metallic liquid, governed by density.

Experimental results for LLIMT serve as starting points for *ab initio* theoretical models. In paper [28], the properties of compressed liquid hydrogen were investigated by means of first-principle molecular dynamics in the pressure range of 75–175 GPa at temperatures close to the melting curve. The results evidence a liquid–liquid transition between molecular and dissociated phases. The transition is accompanied by metallization and a 6% density increase. The calculations assumed protons acting as classical particles.

In the Introduction, we mentioned reasons for the large scattering of analytical results on compressed hydrogen. The situation is the same for numerical approaches. Metallic hydrogen contains no inner screening electrons and a number of structures with similar energies compete with each other. Moreover, a proton is a relatively light particle,

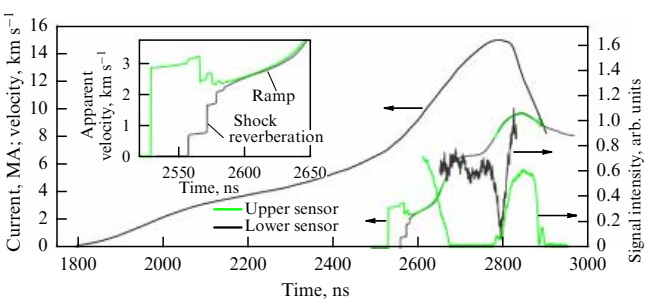

Figure 12. (Color online.) Time dependence of the current (black curve) and relative velocities of aluminum/deuterium (green curve) and deuterium/LiF (grey curve — left axis) interfaces (see also Fig. 10). VISAR signal magnitudes for the reflection from aluminum/deuterium (green curve) and deuterium/LiF (grey curve — right axis) interfaces. The data corresponds to the green experimental trajectory in Fig. 10. (Taken from paper [55].)

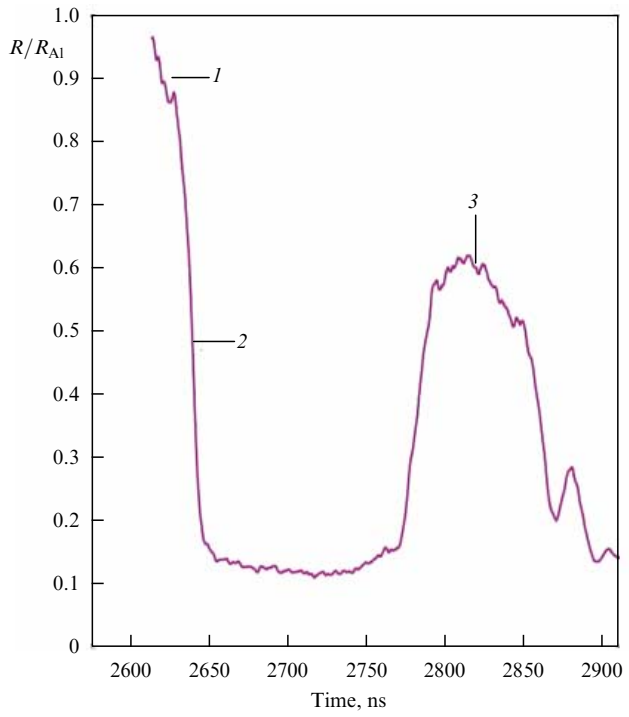

Figure 13. (Color online.) Reflection coefficient R (averaged over wavelength range of 570–610 nm, that is ~ 2.1 eV) normalized to aluminum reflection coefficient R_{Al}. At the beginning (stage *1*), the reflected signal passes through deuterium two times, with reflection from the deuterium/aluminum interface. Later on (stage *2*), the deuterium becomes opaque, as the bandgap energy decreases to 2–2.5 eV and, finally, at stage *3* the sample becomes reflective experiencing the insulator-to-metal transition (IMT) in deuterium. As the pressure is decreased to a value less than the IMT pressure, the reflection from deuterium vanishes. (Taken from Ref. [55].)

and it is incorrect to treat such a particle as a classical one. These circumstances force researchers to go over to progressively more complicated numerical algorithms: to use a semilocal or nonlocal density functional instead of a local one, to use quantum molecular dynamics instead of a classical one, to take into account nuclear effects (that is, the influence of the quantum properties of the proton), and to improve the approaches of the Monte Carlo method.

DFT calculations [29–31] were performed to investigate the region above the melting curve (see Fig. 1). Investigations using semilocal density functionals like the Perdew–Burke–Ernzerhof (PBE) functional indicate the existence of the first-order LLIMT. The transition curve, which starts at the critical point at a temperature of 1500–2000 K and pressure of 120 GPa, has a negative slope of $\mathrm{d}T/\mathrm{d}P$ in the temperature range between 2000 and 800 K. This is the curve in which molecular hydrogen dissociates and transforms into liquid atomic metallic hydrogen. The range of results obtained by different authors is shown in Fig. 1 by two curves connected by horizontal segments. This transition is similar to the PPT, a first-order phase transition in partially ionized plasma [65], but in a dense fluid DFT modeling predicts this transition at a significantly lower temperature and higher pressure (just as predicted for IMT in the solid phase [1]). In later work (see paper [73]), where the authors used first-principle molecular dynamics taking into account nuclear quantum effects (NQEs) and nonlocal functionals, the first-order LLIMT was predicted to appear at pressures larger than 100 GPa (see Fig. 9).

Until recently, DFT methods were employed as a standard tool, because they allow modeling the behavior of a large number of particles with a reasonable computer power consumption. Although all these calculations lead to a first-order LLIMT in a warm dense fluid, the resulting values of P and density ρ are very sensitive to the choice of a method and type of functional. The DFT has a number of disadvantages especially manifested in the case of studies of hydrogen dissociation [76]. First, a single molecule is poorly described both in equilibrium and especially in the dissociation limit. Second, the DFT significantly underestimates electron bandgaps by showing that possible molecular phases can be relatively easily destroyed (by utilizing standard density functionals). Therefore, the DFT is not quite suitable for hydrogen investigations under high pressure, especially in the pressure range which is experimentally inaccessible and for which one cannot check the relevance of invoked functionals.

Among *ab initio* modeling methods, the quantum Monte Carlo method provides the best compromise between accuracy and computer resources, and it appears to be very suitable for the study of the LLIMT problem [76]. However, one needs QMC modeling with a large number of atoms, because otherwise the molecular phase stability is not taken into account properly.

QMC calculations result in LLIMT pressure values, which are 200 GPa larger than the previous DFT calculations [76]. In paper [74] issued in 2015, the QMC method was applied to define the first-order transition curve between a molecular liquid and a mixed molecular–atomic fluid at a finite temperature and pressure of about 400 GPa. The calculation shows a metallic behavior of this mixed phase, which predicts that the metallization takes place significantly earlier than the full atomization of liquid hydrogen (see Fig. 9).

In the experimental paper [55] described above, a sharp LLIMT was observed at $P \simeq 300$ GPa and $\rho \simeq 2.0$–2.1 g cm^{-3}, and at low temperatures. The results [55] set narrow boundaries for the values of P and ρ in the transition and predict that this is a first-order transition that occurs in the region where different variants of DFTs give the most divergent results.

Generally, it can be noticed that both theoretical and experimental results still weakly define the position of the plasma phase transition curve (let us note that the difference between results for hydrogen and deuterium in the framework of the same technique is often much smaller than the results for the same isotope obtained using different methods). However, most recent studies do not eliminate this uncertainty.

For example, in paper [77], where the optical properties of hydrogen were studied at pressures of 10–150 GPa and temperatures up to 6000 K, the possibility of a first-order transition in the mentioned parameter range was ruled out completely. However, in comments made in Ref. [78], an alternative analysis of data from Ref. [77] is presented, with the conclusion that the authors have observed all the same a transition to the metallic state.

In a later comment in Ref. [79], the data of the initial paper [71] have been analyzed once again. The authors of Ref. [79] critically considered the optical data obtained in Ref. [71] and performed their own numerical calculations, which resulted in the conclusion that the high-temperature state studied in Ref. [71] is not metallic, and the data given there cannot distinguish the first-order transition from a continuous

transition or even from the bandgap energy decrease within the same phase.

Summing up, stringent experimental conditions and difficulties in the interpretation of results do not yet allow us to reach final conclusions regarding the LLIMT curve in hydrogen.

3. Silane (SiH_4) under extreme pressures

The possibility of compressed hydrogen metallization was first mentioned in basic paper [1] in 1935. However, the transition of solid hydrogen to the metallic state has not yet been observed experimentally and is a challenging goal. In 2004, Ashcroft [24] assumed that group-IV hydrides are prospective candidates for hydrogen metallization under pressures significantly lower than the ones needed for solid hydrogen, because in hydrides hydrogen is already subjected to 'chemical pressure'. The state-of-the-art of superconductivity research in materials with a high hydrogen content under extreme pressures is given in review [25]. Over the last few years, X-ray, Raman, transport, and infrared techniques for investigations under pressure, as well as theoretical calculations, have been applied to group-IVa hydrides (mainly to silane (SiH_4) and germane (GeH_4)) in order to discover and study their possible metallization and superconductivity.

Silane under pressure was a subject of recent experimental investigations [80]. Raman spectroscopy revealed melting at the pressure of 4 GPa and three crystal–crystal transitions at pressures 6.6, 10, and 26.5 GPa at room temperature. Four high-pressure solid phases were discovered, named III, IV, V, and VI. Infrared measurements have shown an increase in the reflection coefficient as the pressure is increased, starting from 60 GPa [80], which indicates the possibility of metallization at higher pressures according to the prediction made in paper [24]. Theoretical calculations [81] also predict the possibility of silane superconductivity under pressure.

Paper [82] describes in detail the investigation of silane under pressures up to 200 GPa using Raman scattering, measuring the electric resistance, and X-ray diffraction. Molecular silane is reported to transform from an insulating state into metallic state (and at low temperatures into a superconducting state) at a pressure of 50 GPa. Maximum temperature $T_c \approx 17$ K was registered in measurements under pressures of 96 and 120 GPa. Later on, in paper [83], partial decomposition of silane into Si and H_2 was registered at room temperature and 50 GPa. The released hydrogen forms hydrides with materials of a high-pressure cell, in particular, with platinum from which the lead-in wires are made. X-ray spectra of the resulting platinum hydride appear to be the same as the ones measured in Ref. [82] and attributed to the metallic and superconducting phases of silane. These observations have shown the importance of taking into account all possible chemical reactions in high-pressure experiments. Let us also note first-principle calculations [85] according to which at $P = 90$ GPa the PtH-II hydride should be a superconductor with the critical temperature $T_c \simeq 12$ K close to the value of $T_c \simeq 17$ K assigned to silane in paper [82].

Further experiments [84] have revealed silane amorphization for $P > 60$ GPa and the formation of polymerized silane at P of around 100 GPa. According to the conclusions in paper [84], silane does not metalize at a pressure of 60 GPa, despite the results of papers [80, 82]. Instead, for $P > 60$ GPa, it amorphizes. After that, silane recrystallizes for $P > 90$ GPa, forming a phase with a polymer crystalline structure, which agrees with predictions [86]. This means that silane remains nonmetallic at pressures up to $P = 130$ GPa — the maximum pressure reached in paper [84].

The authors of Ref. [87] performed a detailed investigation of the optical, electronic, and structural properties of silane SiH_4 at pressures up to 150 GPa using Raman spectroscopy, optical microscopy, measurements of the infrared reflection coefficient, optical absorption, and diffraction measurements at a synchrotron. In order to eliminate the contamination with metal hydrides, which was reported before in Ref. [83], the experiments were performed in gold-lined gaskets. Silane remained a transparent dielectric with the $P2_1/c$ structure at pressures up to 40 GPa. For $P > 50$ GPa, silane demonstrated partial loss of crystallinity (amorphization) and seemed darkened visibly. In the absence of chemical decomposition, silane remains partially transparent and nonmetallic with the bandgap energy being 0.6–1.8 eV. Under pressure, however, it becomes sensitive to the synchrotron and laser irradiations and easily decomposes, forming metallic silicon.

As the authors of Ref. [87] believe, the results reported in previous publications regarding the metallization of initially molecular SiH_4 are associated with its chemical decomposition, and the superconductivity could have been caused by hydrogen-doped silicon. Large value of T_c observed in Ref. [82] could be related to SiH_x superconducting phases with another stoichiometry or to the silane polymer phase [84].

It is very likely that the superconductivity observed in experiments [82] was supported by superconducting hydride formed in the reaction between platinum measuring electrodes and hydrogen released in the course of partial silane decomposition [85]. The question of silane superconductivity under high pressure, obviously, needs further investigations with side effects taken into account.

Review [25] made in 2015 also systematizes other polyhydrides, for which high values of T_c are predicted.

4. Superconductivity in hydrogen sulfide under pressure at temperature 203 K

It was discovered at the end of the 1990s that hydrogen sulfide (H_2S) transforms into the metallic state at a pressure of about 90 GPa [88], and recently the H_2S superconductivity was predicted at $T = 80$ K [89]. Experiments [90–93] performed in 2014–2015 revealed superconductivity in H_2S (D_2S) with T_c above 200 K and at pressures higher than 90 GPa. The superconductivity was evidenced by a sharp decrease in resistance, a pronounced isotopic effect, a lowering of T_c with the application of a magnetic field, and, finally, the results of magnetic susceptibility investigations, which confirmed the existence of critical temperature $T_c = 203$ K. It was assumed that H_2S decomposes under high pressures into sulphur and H_3S hydride with a higher hydrogen content [91]. It is likely that precisely H_3S transforms into a superconducting state with a highest T_c. Theoretical investigations suggest hydride crystalline structures that can support such large values of T_c [89, 94–97] (all papers published in 2014–2015).

In typical experiments, the loading of the liquid H_2S sample and initial load application were performed at a temperature of 200 K [92]. Raman spectra of H_2S and D_2S measured with the pressure increasing are in good agreement

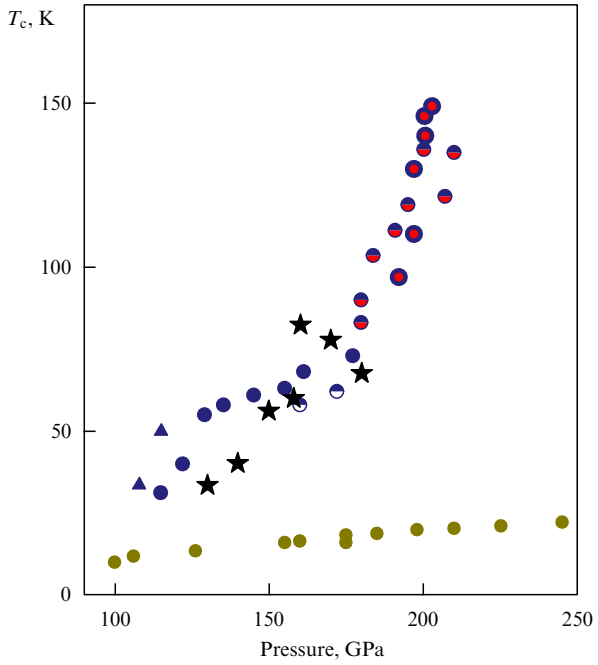

Figure 14. (Color online.) Pressure dependence of T_c in hydrogen sulfide. Blue symbols correspond to T_c in several cycles of a pressure increasing. At pressures above 160 GPa, a more rapid increase in T_c is observed. Black stars mark the calculation results [97], green circles are measured values of T_c for a sulphur sample, obtained using the same four-probe measurement method. (Taken from Ref. [92].)

with the literature [98]. At a pressure of around 50 GPa, the sample is semiconducting (as follows from the temperature dependence and pronounced photoconductivity). At pressures of 90–100 GPa, the conductivity continues to increase and its temperature dependence becomes metallic, while the photoconductivity response vanishes. However, this is a bad metal with a specific resistance of $\sim 3 \times 10^{-5}$ Ω m at $T = 100$ K and $P = 110$ GPa. As the sample is cooled under a pressure of around 100 GPa, the resistance abruptly decreases by 3–4 orders of magnitude, indicating the transition into the superconducting state with $T_c \approx 30$ K. Minimal measured specific resistance $\rho \approx 10^{-11}$ Ω m is two orders of magnitude lower than that of pure copper at $T = 30$ K. Measurements of temperature dependence of sulfur hydride resistance for various pressures revealed an increase in T_c with the increase in pressure, highly pronounced for $P > 160$ GPa (Fig. 14).

In most of the consequent experiments following the loading of the sample and initial application of pressure at $T = 200$ K, the samples were annealed at $P = 150$ GPa and room temperature. This allowed obtaining stable results and defining the dependence of T_c on the pressure and magnetic field in order to prove the emergence of superconductivity. In annealed samples under a pressure increasing, the temperature T_c gradually decreased instead of increasing (Fig. 15). Straight lines in Fig. 15 show that the dependences are parallel at pressures higher than 170 GPa, but greatly diverge at lower pressures.

A strong isotopic effect was also observed in paper [92]. T_c shifts to lower temperatures for sulfur deuteride (Fig. 16), which indicates the phonon superconductivity mechanism, because in the BCS theory the T_c dependence on the atomic mass has the form $T_c \sim m^{-\alpha}$, where $\alpha \approx 0.5$. Comparing values of T_c in the region of a pressure of 170 GPa results in the value of $\alpha \approx 0.3$.

In a magnetic field up to 7 T, the value of T_c shifts to lower temperatures (Fig. 17).

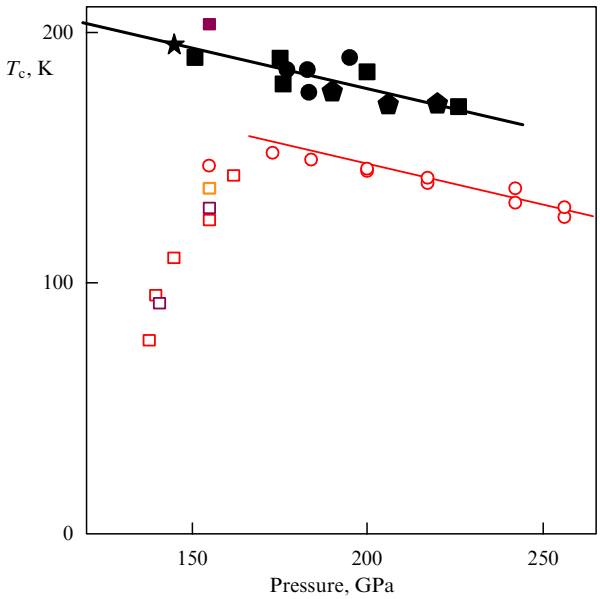

Figure 15. (Color online.) $T_c(P)$ dependence for hydrogen sulfide samples annealed at room temperature. Filled symbols correspond to hydrogen sulfide, and unfilled symbols to deuterium sulfide. Red symbols denote data obtained from magnetic susceptibility measurements. (Taken from Ref. [92].)

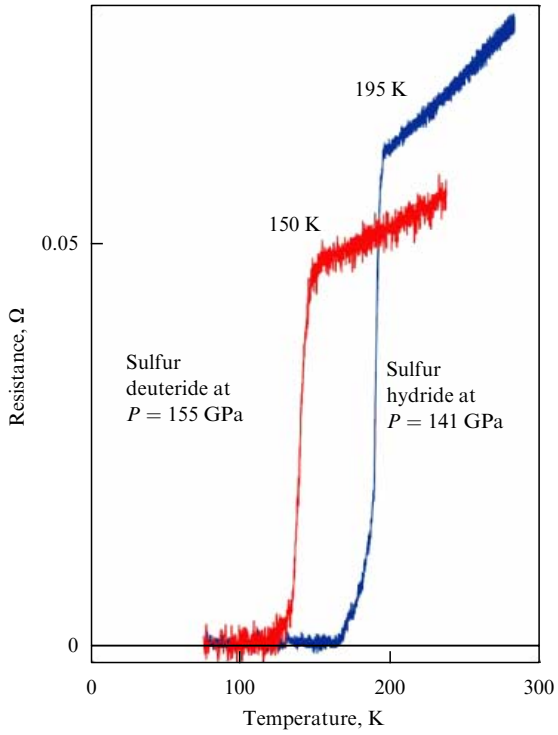

Figure 16. (Color online.) Typical temperature dependences of resistance for sulfur hydride (blue curve) and sulfur deuteride (red curve). Data is obtained during slow heating over a time of several hours. T_c was defined from the sharp resistance increase in the transition to normal metallic behavior. The measurements were performed after annealing the samples at room temperature. (Taken from Ref. [92].)

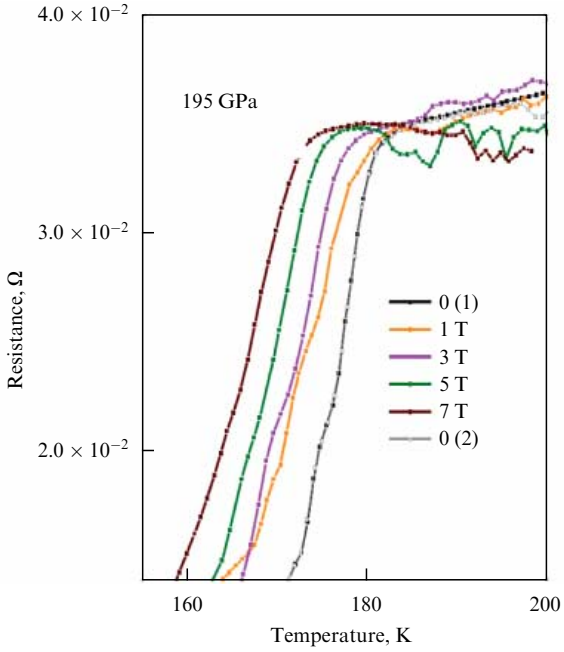

Figure 17. (Color online.) Temperature dependences of sulfur hydride resistance for various magnetic fields and a superconducting transition at $T_c = 185$ K. Zero-field dependences were measured three times: before the application of the magnetic field (black curve — 0(1)), after measurements in fields of 1, 3, 5, 7 T (zero-field dependence in this case is shown by the grey curve — 0(2)), and, finally, after measurements in fields of 2, 4, 6 T (not shown in the figure). (Taken from Ref. [92].)

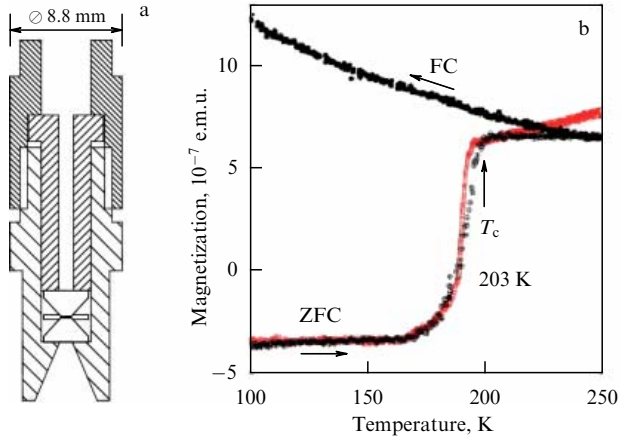

Figure 18. (Color online.) Magnetization measurements: (a) nonmagnetic diamond anvil cell of 8.8-mm in diameter, and (b) temperature dependence of sulfur hydride magnetization at 155 GPa pressure for zero-field cooling (ZFC) and cooling in a 20-Oe field (FC). Origin of the transition — $T_c = 203(1)$ K. For comparison, red dots show a superconducting transition obtained from measurements of electric conductivity at $P = 145$ GPa. The data regarding resistance measurements ($T_c = 195$ K) are scaled and shifted vertically for clarity in comparing with the results of magnetization measurements. The higher value of $T_c = 203$ K obtained from the magnetization measurements can be explained by the contribution of the sample boundaries to the signal: the pressure in those regions is less and T_c is larger than in the center (see Fig. 15). (Taken from Ref. [92].)

Magnetic properties were studied using the magnetic property measurement system (MPMS) by the Quantum Design company. The measurements were performed in a miniaturized nonmagnetic diamond anvil cell made of copper–titanium alloy, operating at pressures up to 200 GPa (Fig. 18a). When measuring the magnetization, a sharp transition from the diamagnetic to paramagnetic state was observed under zero-field cooling (ZFC) (Fig. 18b). The superconducting transition temperature is 203 K, and superconducting transition width is almost the same as in measurements of electric conductivity. Magnetization measurements $M(H)$ at various temperatures demonstrate a pronounced hysteresis loop, indicating type II superconductivity with the lower critical field $H_{c1} < 30$ mT. Magnetization sharply decreases at temperatures above 200 K [92].

Summing up, paper [92] presents experimental evidence of the H_2S transition to the superconducting state. However, H_2S decomposes under pressure into polyhydrides and sulfur. In order to define which of these substances has a maximum value of T_c, the authors of Ref. [92] referred to theoretical work.

The authors related the results obtained for unannealed samples to the initial H_2S compound, because they are as a whole in good agreement with the calculated results [97] with respect to both the temperature $T_c \sim 80$ K and the pressure dependence $T_c(P)$ character (see Fig. 14).

On the other hand, maximum values of $T_c \approx 200$ K obtained for annealed samples are connected in Ref. [92] with H_2S decomposition at room temperature. Such decomposition can result in sulfur precipitation for $P < 100$ GPa [99]. The superconducting transition occurs in elementary sulfur at significantly lower temperatures than in H_2S (see Fig. 14). Another expected decomposition product is hydrogen. However, the Raman spectrum did not indicate a characteristically strong vibron corresponding to stretch vibrations in the H_2 molecule. Therefore, it was assumed in paper [92] that H_2S dissociation proceeds with the production of higher hydrides. This assumption is supported by the theoretical study [89], where it was shown that at pressures above 180 GPa the van der Waals compound $(H_2S)_2H_2$ forms a structure with H_3S stoichiometry. The predicted value of $T_c \approx 190$ K and its dependence on pressure [89] are close to available experimental data (see Fig. 15). The hypothesis of the authors of Refs [90, 92] about the H_2S transformation to higher hydrides (and sulfur) was supported by follow-up calculations [94, 95]. All numerical investigations are based on the $Im\bar{3}m$ structure (Fig. 19), giving the same estimate for $T_c \sim 200$ K and predicting a T_c decrease with the pressure increase.

The calculations show that the main contribution to H_3S superconductivity is provided by the hydrogen sublattice [89, 100]. By taking into account zero-point vibrations and anharmonicity, the calculations in Ref. [96] resulted in a corrected T_c value of 190 K, and consideration of the isotopic effect changes the exponent α from 0.5 to 0.35, which is all in agreement with experimental results [92].

The highest value of T_c, equal to 203 K, reported in paper [92] was, most likely, obtained for H_3S with the $Im\bar{3}m$ structure. This is a good metal; it contains strong covalent bonds between H and S atoms [89]. Such properties agree with the general assumption that metals with high T_c must possess strong covalent bonds and high-frequency modes in the phonon spectrum (as in MgB_2 [101]). This can be an effective criterion in the search for materials with high T_c.

Paper [102] published in 2016 is a natural continuation of the main experimental work [92] and it expands the variety of methods used for the investigation of the hydrogen sulfide state with $T_c \approx 200$ K (Figs 20, 21). The fabrication of a

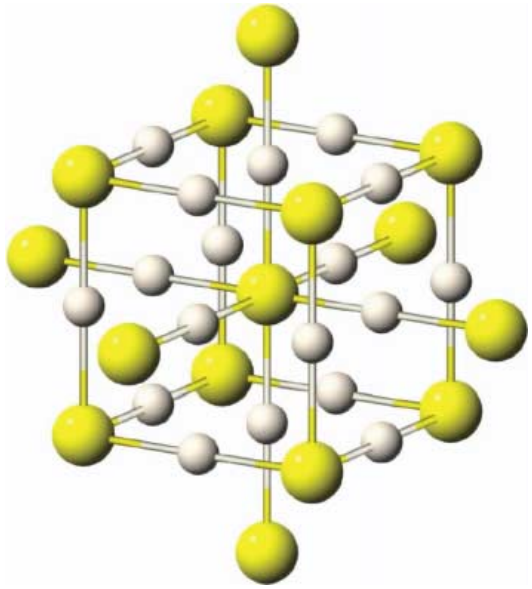

Figure 19. $Im\bar{3}m$ crystalline structure of H_3S, illustrating two alternating ReO_3 type sublattices. Large spheres refer to S, and small ones to H. (Taken from Ref. [100].)

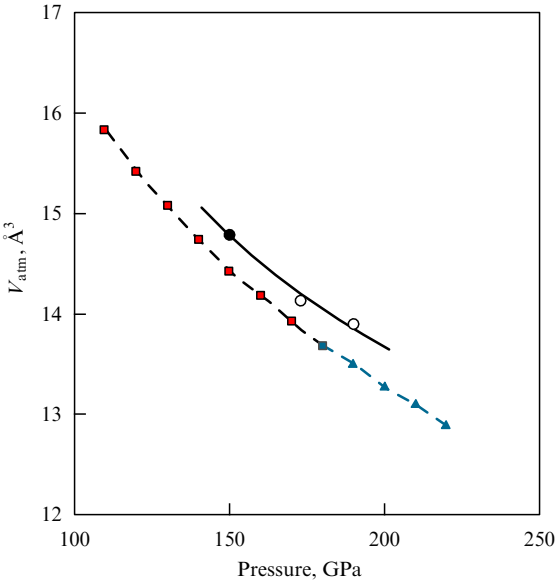

Figure 20. (Color online.) Pressure dependence of the atomic volume for sulfur hydride and sulfur deuteride (filled and unfilled circles, respectively). Experimental data obtained during the pressure increase are approximated by the first-order Birch equation of state (solid curve). Theoretically predicted volumes for a hexagonal structure (R3m) and a bcc structure ($Im\bar{3}m$) are shown by red squares and green triangles, respectively [89]. (Taken from Ref. [102].)

sample in DAC and resistance measurements are performed similarly to those in Ref. [92]. Crystalline structures of superconducting compressed H_2S and D_2S are obtained in synchrotron studies with a simultaneous measurement of resistance at room and lower temperatures.

Paper [102] presents the results of simultaneous measurements of X-ray spectra and electric resistance for sulfur deuteride under a pressure of 173 GPa in the temperature range of 13–300 K. X-ray spectra remain unchanged in the whole temperature region, while the resistance demonstrates

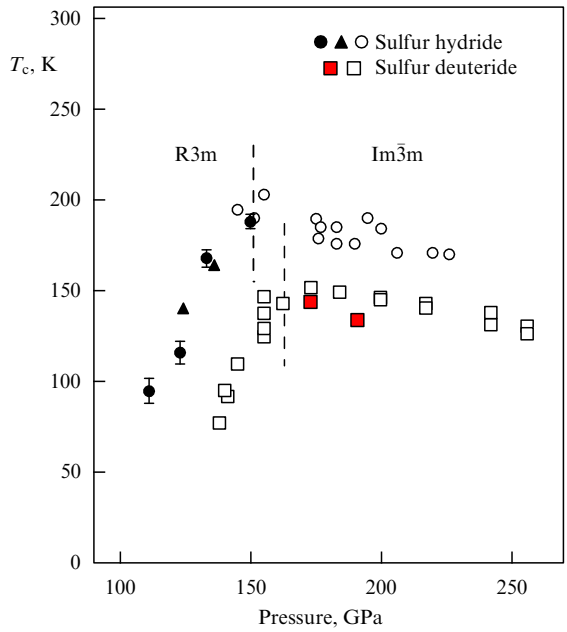

Figure 21. (Color online.) Pressure dependences of the critical temperature for sulfur hydride and sulfur deuteride. Unfilled circles and squares label the results of paper [92], and filled symbols refer to Ref. [102]: circles correspond to data obtained while decreasing the pressure, squares and triangles while increasing the pressure. Dashed curves indicate the boundary between the phases with R3m and $Im\bar{3}m$ structures. (Taken from Ref. [102].)

a rapid decrease, which corresponds to a superconducting transition at temperatures below 150 K. It is discovered that the superconducting phase structure is mainly (as far as it can be defined by powder X-ray spectra) in good agreement with the theoretically predicted body-centered hexagonal and cubic phases [89] and that it coexists with elementary sulfur. This confirms the fact that compression results in the reaction $3H_2S \rightarrow 2H_3S + S$.

X-ray spectra allow the conclusion that, under pressure, molecular hydrogen sulfide H_2S (D_2S) decomposes, according to theoretical predictions, into molecular H_3S (D_3S) with a body-centered cubic (bcc) structure and sulfur with a β-Po structure.

What was previously presented as proof of the superconducting state — abrupt resistance decrease, isotopic effect, T_c decrease in a magnetic field, and, finally, results of magnetic susceptibility measurements, which confirmed the existence of $T_c = 203$ K [92] — is now completed with X-ray measurements of the superconducting phase structure [102]. X-ray data do not contradict theoretical predictions.

The final confirmation of the hydrogen sulfide superconducting state would have been the observation of the Meissner effect — the expulsion of a magnetic field from the sample as it transforms into a superconducting state. The authors of Ref. [103] report an effective screening of the external magnetic field by a superconducting H_2S sample (at 153 GPa pressure) on a ^{119}Sn sensor (Fig. 22a). As the sensor, the researchers used tin foil 2.6 μm in thickness enriched up to 95% with the ^{119}Sn isotope. The sensor was placed in the DAC gasket opening before loading the H_2S sample to a cell. The magnetic field is detected by magnetic interaction between ^{119}Sn nuclei, which is measured by nuclear resonance scattering (NRS) of synchrotron radiation [104]. The existence of a magnetic field near tin nuclei was defined by

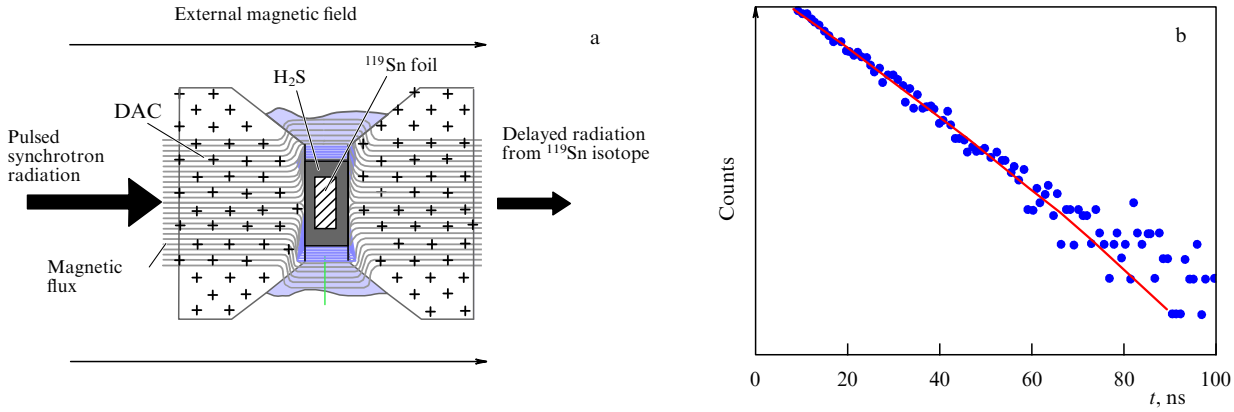

Figure 22. (Color online.) (a) Experimental setup [103]. Tin foil surrounded by compressed hydrogen sulfide is located in a DAC under a pressure of about 153 GPa. A magnetic field is directed along the synchrotron radiation. Pulsed synchrotron radiation excites the nuclei of the ^{119}Sn Mössbauer isotope. The detection system measures the time dependence of tin nuclei radiation emitted in the forward direction. (b) Nuclear resonance scattering spectrum for ^{119}Sn in H_2S at $T = 59$ K and $P = 153$ GPa. External magnetic field $H_{ext} = 0.68$ T. For $T < T_c$, the tin foil is screened from the external magnetic field by the superconducting hydrogen sulfide, so the nuclear energy levels do not split and there are no quantum beatings in the spectra. (Taken from Ref. [103].)

quantum beatings in time-resolved NRS spectra [105]. The resonant character of NRS guarantees that the accumulated data will depend only on the ^{119}Sn sensor with zero environmental background.

The method suggested in paper [103] resulted in the observation of superconductivity in the studied hydrogen sulfide samples. The measurement procedure was the following. First, the sample was cooled in a zero magnetic field (ZFC) to the temperature of 5 K and then the magnetic field of around 0.7 T was applied. Since the H_2S sample resides in a superconducting state at $P = 153$ GPa and $T = 5$ K, the field did not penetrate the sample and did not influence the sensor — quantum beatings in time-resolved NRS spectra were absent (Fig. 22b). After that, the temperature was gradually increased, and the NRS spectra were recorded.

As the temperature was increased, the appearance of quantum beatings indicated first partial and then full disappearance of sensor screening from the external magnetic field (Fig. 23a). In the same series of experiments, NRS spectra were measured in external magnetic field $H_{ext} = 0.68$ T at temperatures of 4.7 and 14 K for a similar setup with the ^{119}Sn sensor in the same cell, but with the H_2 sample under pressure $P = 150$ GPa. Quantum beatings were observed already at the lowest temperature (4.7 K), which

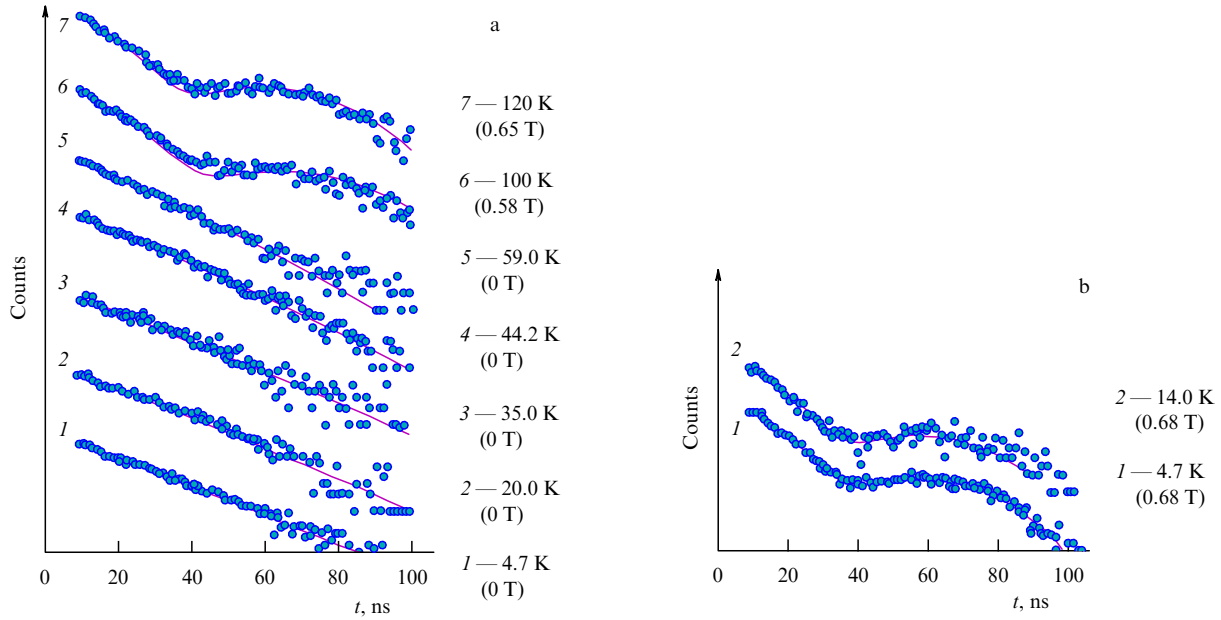

Figure 23. (Color online.) NRS spectra measured by an ^{119}Sn sensor in H_2S under a pressure of 153 GPa, external magnetic field of 0.68 T directed normal to the tin detector surface, and temperatures in the range from 4.7 to 120 K. Each spectrum is marked with the values of temperature and magnetic field on the nuclei (in brackets). (a) Purely exponential decay seen in curves *1–5* shows that there is no magnetic field on ^{119}Sn nuclei. This proves that the external magnetic field cannot penetrate H_2S and, hence, H_2S is superconducting. At $T \approx 100$ K, pronounced oscillations start to show themselves (quantum beatings), indicating the presence of a magnetic field at the sensor. (b) NRS spectra for a reference sample in the same measurements cycle and the same external field at temperatures of 4.7 and 14 K. Similar setup with an ^{119}Sn sensor in the same cell, but with the H_2 sample at $P = 150$ GPa. Quantum beatings were observed already at the lowest temperature of 4.7 K, which points to the absence of sensor screening from the external magnetic field. (Taken from Ref. [103].)

indicates the absence of sensor screening from the magnetic field.

Experimental results demonstrate that the H_2S superconducting sample efficiently screens the magnetic field of ~ 0.7 T at temperatures up to $T \sim 100$ K. Partial screening of the magnetic field remains at temperatures up to at least 140 K. This confirms that the investigated H_2S sample compressed at 153 GPa is a superconductor with high critical parameters. Preparation of the hydrogen sulfide sample is an important part of the experiment and is described in detail in supplementary materials to paper [103]. The pressure was increased to 153 GPa for $T < 240$ K in order to prevent sample decomposition. After that, the sample was heated to room temperature. The sample used in Ref. [103] was stored at room temperature and a pressure of 153 GPa for over a week.

When comparing the data presented in papers [92, 103], it should be noted that the resistance measurements detect the very beginning of the current flow, while the magnetic measurements need a larger part of the sample to be in a superconducting state.

For a long period of time, the results of work [90–92, 102, 103] were not repeated in other experiments. The first independent confirmation of the results mentioned above appeared in paper [109], where the superconductivity in H_2S was registered by magnetic susceptibility measurements at pressures above 117 GPa with maximal $T_c = 183$ K at a pressure of 149 GPa.

In Ref. [110], hydrogen sulfide was investigated by means of X-ray diffraction and Raman spectroscopic methods. Superconductivity was not observed, but the investigation of the same $P-T$ paths as in Ref. [92] allowed the mechanisms of chemical and physical transformations to be clarified. In particular, it was confirmed that superconductivity with high T_c originates from the H_3S hydride that forms under pressure.

The first spectroscopic study of a new superconductor is presented in Ref. [111]. Reflection coefficients were measured for photons with energies in the range from 60 to 600 meV at pressures up to 150 GPa and for several temperatures. The results are in agreement with calculations based on the Eliashberg equation, which is considered evidence for the phonon mechanism of pairing.

5. Conclusions

Intensive studies carried out in 2014–2016 resulted in significant changes to the hydrogen phase diagram, which is clear from a comparison of Fig. 1 with Figs 5, 7, 8. Static experiments give some indications of possible hydrogen metallization on approaching the pressure of 400 GPa. However, a lot of work is needed in order to obtain convincing data. In particular, resistance needs to be measured using a four-probe setup.

Shock wave experiments resulted in more reliable indications of reaching metallic conductivity — the liquid–liquid insulator-to-metal transition (LLIMT) in deuterium at temperatures of 100–2000 K and pressures of about 300 GPa.

Superconductivity has been discovered in H_2S (D_2S) at pressures above 90 GPa and with critical temperatures above 200 K. The superconducting state is proved by the abrupt decrease in the electric resistance, clearly pronounced isotopic effect, decrease in T_c with application of the magnetic field, and, finally, results of magnetic susceptibility measurements and observation of external magnetic field screening. Experimental investigations of hydrogen sulfide superconductivity stimulated the publication of a large number of theoretical papers.

The discovery of sulfur hydride superconductivity fueled the search for superconductivity in other hydrides and led to its discovery in phosphorus hydride (PH_3) with quite high T_c (around 100 K) at 200 GPa pressure [112]. The results of systematic theoretical investigations of solid PH_3 performed in Ref. [113] predict two stable superconducting structures in the pressure range of 100–200 GPa. For the monoclinic structure (C2/m) it is predicted that $T_c = 83$ K at 200 GPa pressure, which is in perfect agreement with experimental data [112]. Calculations exploiting the evolution algorithm together with the density functional theory [114] predict the existence of stable phosphorous hydrides (PH_n, $n = 1-6$). It turned out that during hydride decomposition three metallic PH_2 phases are stable. Phases with I4/mmm and 2FU-C2/m structures are the most stable and result in the calculated superconducting transition temperatures of 60 and 76 K at a pressure of around 200 GPa. The results of these calculations agree with the experimental results [112]. Finally, the application of rapid cooling methods to samples in the temperature range from the synthesis temperature of 300 °C to the liquid-nitrogen temperature resulted in the discovery of superconducting transitions with $T_c = 50-60$ K in metastable PdH_x and PdD_x samples with $x \sim 0.5$ [115]. These palladium–hydrogen systems, it would seem, has been studied in detail, and the maximum values of $T_c \sim 9-11$ K were obtained earlier for $x = 1$.

The results achieved are mostly due to progress in experimental methods for extremely high pressures. A pressure range up to 400 GPa has been achieved in single-stage cells with diamond anvils. Authors utilized conventional diamond anvils with a small working area diameter (30–60 μm), a 7–8° bevel, and a diameter of about 200 μm [103]. In individual experiments [61, 62], a record-high pressure of $P \approx 500$ GPa has been obtained for hydrogen. This was achieved by giving up continuous control over pressure (even a small measurement signal can destroy the strained diamonds) and measuring it only at the final point. Over the last few years, a research technique using a two-stage DAC has been improved [106, 107]. This method is intended to achieve a pressure range up to 1000 GPa, and it has already been used for X-ray studies of the structure and equation of state in osmium under a pressure up to 750 GPa [108].

Acknowledgments

The authors are deeply grateful to S M Stishov and V V Brazhkin for their stimulating discussions.

References

1. Wigner E, Huntington H B *J. Chem. Phys.* **3** 764 (1935)
2. Abrikosov A A *Astron. Zh.* **31** 112 (1954)
3. Abrikosov A A *Sov. Phys. JETP* **12** 1254 (1961); *Zh. Eksp. Teor. Fiz.* **39** 1797 (1960)
4. Abrikosov A A *Sov. Phys. JETP* **14** 408 (1962); *Zh. Eksp. Teor. Fiz.* **41** 569 (1961)
5. Abrikosov A A *Sov. Phys. JETP* **18** 1399 (1964); *Zh. Eksp. Teor. Fiz.* **45** 2038 (1963)
6. Trubitsyn V P *Sov. Phys. Solid State* **7** 2708 (1966); *Fiz. Tverd. Tela* **7** 3363 (1965)
7. Trubitsyn V P *Sov. Phys. Solid State* **8** 688 (1966); *Fiz. Tverd. Tela* **8** 862 (1966)
8. Ashcroft N W *Phys. Rev. Lett.* **21** 1748 (1968)

9. Brovman E G, Kagan Yu, Kholas A *Sov. Phys. JETP* **34** 1300 (1972); *Zh. Eksp. Teor. Fiz.* **61** 2429 (1971)
10. Brovman E G, Kagan Yu, Kholas A *Sov. Phys. JETP* **35** 783 (1972); *Zh. Eksp. Teor. Fiz.* **62** 1492 (1972)
11. Oliva J, Ashcroft N W *Phys. Rev. B* **23** 6399 (1981)
12. Schneider T *Helv. Phys. Acta* **42** 957 (1969)
13. McMahon J M et al. *Rev. Mod. Phys.* **84** 1607 (2012)
14. Mao H, Hemley R J *Rev. Mod. Phys.* **66** 671 (1994)
15. Maksimov E G, Shilov Yu I *Phys. Usp.* **42** 1121 (1999); *Usp. Fiz. Nauk* **169** 1223 (1999)
16. Nellis W J *Rep. Prog. Phys.* **69** 1479 (2006)
17. Nellis W J *High Pressure Res.* **33** 369 (2013)
18. Trunin R F, Urlin V D, Medvedev A B *Phys. Usp.* **53** 577 (2010); *Usp. Fiz. Nauk* **180** 605 (2010)
19. Loubeyre P et al. *High Pressure Res.* **24** 25 (2004)
20. Loubeyre P et al. *Phys. Rev. B* **86** 144115 (2012)
21. Goncharov A F, Howie R T, Gregoryanz E *Low. Temp. Phys.* **39** 402 (2013); *Fiz. Niz. Temp.* **39** 523 (2013)
22. Ginzburg V L *Sov. Phys. Usp.* **14** 21 (1971); *Up. Fiz. Nauk* **103** 87 (1971)
23. Silvera I *Proc. Natl. Acad. Sci. USA* **107** 12743 (2010)
24. Ashcroft N W *Phys. Rev. Lett.* **92** 187002 (2004)
25. Struzhkin V V *Physica C* **514** 77 (2015)
26. Bonev S A et al. *Nature* **431** 669 (2004)
27. Attaccalite C, Sorella S *Phys. Rev. Lett.* **100** 114501 (2008)
28. Scandolo S *Proc. Natl. Acad. Sci. USA* **100** 3051 (2003)
29. Lorenzen W, Holst B, Redmer R *Phys. Rev. B* **82** 195107 (2010)
30. Morales M A et al. *Proc. Natl. Acad. Sci. USA* **107** 12799 (2010)
31. Tamblyn I, Bonev S A *Phys. Rev. Lett.* **104** 065702 (2010)
32. Dzyabura V, Zaghoo M, Silvera I F *Proc. Natl. Acad. Sci. USA* **110** 8040 (2013)
33. Fortov V E et al. *Phys. Rev. Lett.* **99** 185001 (2007)
34. Eremets M I, Trojan I A *JETP Lett.* **89** 174 (2009); *Pis'ma Zh. Eksp. Teor. Fiz.* **89** 198 (2009)
35. Deemyad S, Silvera I F *Phys. Rev. Lett.* **100** 155701 (2008)
36. Subramanian N et al. *Proc. Natl. Acad. Sci. USA* **108** 6014 (2011)
37. Weir S T, Mitchell A C, Nellis W J *Phys. Rev. Lett.* **76** 1860 (1996)
38. Howie R T, Dalladay-Simpson P, Gregoryanz E *Nature Mater.* **14** 495 (2015)
39. Kechin V V et al. *Sov. Phys. JETP* **45** 182 (1977); *Zh. Eksp. Teor. Fiz.* **72** 345 (1977)
40. Liebenberg D H, Mills R L, Bronson J C *Phys. Rev. B* **18** 4526 (1978)
41. Diatschenko V, Chu C W *Bull. Am. Phys. Soc.* **26** 322 (1981); *Science* **212** 1393 (1981)
42. Diatschenko V et al. *Phys. Rev. B* **32** 381 (1985)
43. Datchi F, Loubeyre P, LeToullec R *Phys. Rev. B* **61** 6535 (2000)
44. Gregoryanz E et al. *Phys. Rev. Lett.* **90** 175701 (2003)
45. Akahama Y, Kawamura H *J. Appl. Phys.* **100** 043516 (2006)
46. Howie R T et al. *Phys. Rev. Lett.* **108** 125501 (2012)
47. Kechin V V *Phys. Rev. B* **65** 052102 (2001)
48. Liu H et al. *J. Phys. Chem. C* **117** 11873 (2013)
49. Chen J et al. *Nature Commun.* **4** 2064 (2013)
50. Babaev E, Sudbø A, Ashcroft N W *Nature* **431** 666 (2004)
51. Mazin I I et al. *Phys. Rev. Lett.* **78** 1066 (1997)
52. Pickard C J, Martinez-Canales M, Needs R J *Phys. Rev. B* **85** 214114 (2012)
53. Drummond N D et al. *Nature Commun.* **6** 7794 (2015)
54. Dalladay-Simpson P, Howie R T, Gregoryanz E *Nature* **529** 63 (2016)
55. Knudson M D et al. *Science* **348** 1455 (2015)
56. Eremets I M, Troyan I A, Drozdov A P, arXiv:1601.04479
57. Eremets M I, Troyan I A *Nature Mater.* **10** 927 (2011)
58. Goncharov A F et al. *Phys. Rev. B* **87** 024101 (2013)
59. Liu H, Wang H, Ma Y *J. Phys. Chem. C* **116** 9221 (2012)
60. Dias R, Noked O, Silvera I F, arXiv:1603.02162
61. Dias R, Silvera I F, arXiv:1610.01634
62. Dias R P, Silvera I F *Science* **355** 715 (2017)
63. Zha C et al. *Phys. Rev. Lett.* **110** 217402 (2013)
64. Loubeyre P, Occelli F, LeToullec R *Nature* **416** 613 (2002)
65. Landau L D, Zeldovich Ya B *Acta Physicochim. USSR* **18** 194 (1943); *Zh. Eksp. Teor. Fiz.* **14** 32 (1944)
66. Norman G E, Starostin A N *Teplofiz. Vys. Temp.* **6** 410 (1968)
67. Nellis W J, Weir S T, Mitchell A C *Phys. Rev. B* **59** 3434 (1999)
68. Collins L A et al. *Phys. Rev. B* **63** 184110 (2001)
69. Holst B, Redmer R, Desjarlais M P *Phys. Rev. B* **77** 184201 (2008)
70. Ohta K et al. *Sci. Rep.* **5** 16560 (2015)
71. Zaghoo M, Salamat A, Silvera I F *Phys. Rev. B* **93** 155128 (2016)
72. Zaghoo M, Salamat A, Silvera I F, arXiv:1504.00259
73. Morales M A et al. *Phys. Rev. Lett.* **110** 065702 (2013)
74. Mazzola G, Sorella S *Phys. Rev. Lett.* **114** 105701 (2015)
75. Reisman D B et al. *Phys. Rev. ST Accel. Beams* **18** 090401 (2015)
76. Mazzola G, Yunoki S, Sorella S *Nature Commun.* **5** 3487 (2014)
77. McWilliams R S et al. *Phys. Rev. Lett.* **116** 255501 (2016)
78. Silvera I F et al., arXiv:1608.04479
79. Goncharov A F, Geballe Z M *Phys. Rev. B* **96** 157101 (2017); arXiv:1611.08875
80. Chen X-J et al. *Proc. Natl. Acad. Sci. USA* **105** 20 (2008)
81. Chen X-J et al. *Phys. Rev. Lett.* **101** 077002 (2008)
82. Eremets M I et al. *Science* **319** 1506 (2008)
83. Degtyareva O et al. *Solid State Commun.* **149** 1583 (2009)
84. Hanfland M et al. *Phys. Rev. Lett.* **106** 095503 (2011)
85. Scheler T et al. *Phys. Rev. B* **83** 214106 (2011)
86. Pickard C J, Needs R J *Phys. Rev. Lett.* **97** 045504 (2006)
87. Strobel T A et al. *Phys. Rev. B* **83** 144102 (2011)
88. Sakashita M et al. *Phys. Rev. Lett.* **79** 1082 (1997)
89. Duan D et al. *Sci. Rep.* **4** 6968 (2014)
90. Drozdov A P, Eremets M I, Troyan I A, arXiv:1412.0460
91. Drozdov A P et al., arXiv:1506.08190
92. Drozdov A P et al. *Nature* **525** 73 (2015)
93. Eremets M I, Drozdov A P *Phys. Usp.* **59** 1154 (2016); *Usp. Fiz. Nauk* **186** 1257 (2016)
94. Duan D et al. *Phys. Rev. B* **91** 180502(R) (2015)
95. Bernstein N et al. *Phys. Rev. B* **91** 060511(R) (2015)
96. Errea I et al. *Phys. Rev. Lett.* **114** 157004 (2015)
97. Li Y et al. *J. Chem. Phys.* **140** 174712 (2014)
98. Shimizu H et al. *Phys. Rev. B* **51** 9391(R) (1995)
99. Fujihisa H et al. *Phys. Rev. B* **69** 214102 (2004)
100. Papaconstantopoulos D A et al. *Phys. Rev. B* **91** 184511 (2015)
101. An J M, Pickett W E *Phys. Rev. Lett.* **86** 4366 (2001)
102. Einaga M et al. *Nature Phys.* **12** 835 (2016); arXiv:1509.03156
103. Troyan I et al. *Science* **351** 1303 (2016)
104. Gerdau E, DeWaard H *Hyperfine Interact.* **123–124** 0 (1999)
105. Hastings J B et al. *Phys. Rev. Lett.* **66** 770 (1991)
106. Dubrovinsky L et al. *Nature Commun.* **3** 1163 (2012)
107. Sakai T et al. *Rev. Sci. Instrum.* **86** 033905 (2015)
108. Dubrovinsky L et al. *Nature* **525** 226 (2015)
109. Huang X et al., arXiv:1610.02630
110. Goncharov A F et al. *Phys. Rev. B* **93** 174105 (2016)
111. Capitani F et al. *Nature Phys.* **13** 859 (2017); arXiv:1612.06732
112. Drozdov A P, Eremets M I, Troyan I A, arXiv:1508.06224
113. Liu H et al. *J. Phys. Chem. C* **120** 3458 (2016)
114. Shamp A et al. *J. Am. Chem. Soc.* **138** 1884 (2016)
115. Syed H M et al., arXiv:1608.01774